RESEARCH ARTICLE | OCTOBER 07 2024

Quantification and assessment of the atmospheric boundary layer height measured during the AWAKEN experiment by a scanning LiDAR

Special Collection: **Preparatory work for the American Wake Experiment (AWAKEN)**

M. Puccioni ✉ iD ; C. F. Moss iD ; M. S. Solari iD ; S. Roy iD ; G. V. Iungo iD ; S. Wharton iD ; P. Moriarty iD

Check for updates

View Online

Export Citation

Articles You May Be Interested In

Characterization of wind speed and directional shear at the AWAKEN field campaign site

J. Renewable Sustainable Energy (June 2023)

Overview of preparation for the American WAKE ExperimeNt (AWAKEN)

J. Renewable Sustainable Energy (October 2024)

Tilted lidar profiling: Development and testing of a novel scanning strategy for inhomogeneous flows

J. Renewable Sustainable Energy (August 2024)

Quantification and assessment of the atmospheric boundary layer height measured during the AWAKEN experiment by a scanning LiDAR

M. Puccioni,[1,a)] (iD) C. F. Moss,[2] (iD) M. S. Solari,[2] (iD) S. Roy,[2] (iD) G. V. Iungo,[2] (iD) S. Wharton,[1] (iD) and P. Moriarty[3] (iD)

AFFILIATIONS

[1]Atmospheric, Earth and Energy Division, Lawrence Livermore National Laboratory, 7000 East Ave, Livermore, California 94550, USA

[2]Wind Fluids and Experiments (WindFluX) Laboratory, Mechanical Engineering Department, The University of Texas at Dallas, 800 W Campbell Rd., Richardson, Texas 75080, USA

[3]National Renewable Energy Laboratory, Golden, Colorado 80401, USA

Note: This article is part of the special issue Preparatory Work for the American Wake Experiment (AWAKEN).
[a)]Author to whom correspondence should be addressed: puccioni2@llnl.gov

ABSTRACT

The atmospheric boundary layer (ABL) height plays a key role in many atmospheric processes as one of the dominant flow length scales. However, a systematic quantification of the ABL height over the entire range of scales (i.e., with periods ranging from one minute to one year) is still lacking in literature. In this work, the ABL height is quantified based on high-resolution measurements collected by a scanning pulsed Doppler LiDAR during the recent American WAKE experimeNt (AWAKEN) campaign. The high availability of ABL height estimates (≈ 2200 collected over one year and each of them based on 10-min averaged statistics) allows to robustly assess five different ABL height models, i.e., one for convective thermal conditions and four for stable conditions. Thermal condition is quantified by a stability parameter spanning three orders of magnitude and probed by near-ground 3D sonic anemometry. The free-atmosphere stability, quantified by the Brunt–Väisälä frequency, is both calculated from simultaneous radiosonde measurements and obtained from the best fit of two of the chosen ABL height models. Good agreement is found between the data and three of the chosen models, quantified by mean absolute errors on the ABL height between 281 and 585 m. Furthermore, the seasonal variability of the convective ABL height model parameters (-15% to $+23\%$ with respect to the year baseline) agrees with the variability of buoyancy-generated turbulence caused by the variation in solar radiation throughout the year.

I. INTRODUCTION

The atmospheric boundary layer (ABL), i.e., the lowest portion of the Earth's atmosphere affected by the presence of the ground via surface drag and energy exchange,[1,2] is characterized by complex turbulence processes impacting several fields such as pollutant transport,[3] numerical weather prediction,[4] air quality,[5] and wind[6] and solar energy.[7] A deep understanding of the physical processes within the ABL is rooted in reliable experimental measurements up to the ABL height [$z_i \approx \mathcal{O}(1000)$ m], which represents one of the fundamental scaling parameters governing the turbulence dynamics in the atmosphere.[1,8,9] A key feature of this parameter is its large variability over a wide range of timescales, spanning from minutes-long[1] to several months[10] and years.[11] To address this feature, accurate predictive models of the ABL height are available in the literature to capture the

effect of either positive[12,13] or negative[14–18] vertical heat flux, as well as free-flow stratification in the troposphere,[19,20] high-latitudes,[21] and complex terrain effects. A caveat of these studies, however, is the limited amount of high-quality experimental data (on the order of few tens of data points along the vertical direction,[22] typically collected by 3D sonic anemometry) against which the ABL height models are assessed, mainly due to the relatively short duration of the experimental campaigns (e.g., a few months).[23,24]

From the experimental standpoint, a suitable way to determine the ABL height involves diagnosing vertical turbulent statistics evolving along the vertical direction (z) and rapidly changing across the ABL height, and calibrating some empirical models dependent on z and using z_i as a free parameter.[25] Several diagnostic methods are available in the literature according to the physical mechanisms driving

the ABL evolution throughout the day. In particular, the daytime ABL height can be determined based on mean thermodynamic profiles,[26] mean backscatter coefficient (which keeps track of the local aerosol concentration),[27–31] backscatter-to-extinction coefficient ratio,[32] backscatter coefficient variance,[33] vertical velocity variance,[34] and turbulent shear stress,[35] i.e., statistical quantities reflecting a high turbulence intensity within the ABL and a subsequent sharp decrease moving into the free troposphere. By contrast, the nocturnal ABL, constituted by a thin shear layer (of the order of few hundreds of meters) closer to the ground and capped by a residual layer aloft, is more challenging to probe due to the low turbulence level and the presence of non-canonical ABL events. Thus, retrieval methods for the stable ABL height seek local maxima of the mean velocity[36,37] as well as local minima of streamwise[37] or vertical velocity[38] fluctuations.

In this scenario, a breadth of experimental instruments are commonly used to determine the ABL height experimentally, such as radiosondes,[39,40] ceilometers,[31] and optical sensing techniques.[10,26,27,40–42] Among the latter, the scanning pulsed Doppler light detection and ranging (LiDAR) technology has gained importance in estimating the ABL height due to its extended measurement range (over 2000 m) together with its high spatiotemporal resolution (≈ 20 m, ≈ 1s, respectively) (see, e.g., Refs. 25, 30, and 43–46). Several diagnostic techniques have been developed to quantify the ABL height based on LiDAR-retrieved quantities, such as wavelet covariance transform,[10,28–30] image processing,[47] empirical models,[27,48] and gradient[44] and variance methods.[33] However, the accuracy of these methods relies upon months- to years-long experimental campaigns to quantify the variability of z_i with adequate statistical convergence.

To address several research questions in the wind energy field, the multi-institutional American WAKE experimeNt (AWAKEN) campaign was recently conducted in the Southern Great Plains (SGP) in Oklahoma, U.S., from 2022 to 2024.[49,50] One of the main goals of this campaign is to study the mutual interaction between the ABL and five closely spaced wind farms under different micro-meteorological conditions. This goal, in turn, requires a systematic and reliable quantification of the ABL height over the entire range of energy-containing turbulent scales. Thus, in this work, a novel dataset of ABL height measurements is presented based on data collected by one ground-based scanning LiDAR deployed during the AWAKEN campaign. In particular, high-frequency, quality-controlled LiDAR measurements of vertical velocity and signal-to-noise ratio are used to estimate z_i under a wide range of thermal and shear conditions, the latter quantified by high-frequency single-point 3D sonic anemometer measurements close to the ground. Given the large number of available ABL height estimates, the present analysis aims to obtain a robust assessment of five ABL height predictive models available from the literature (both in stable and convective conditions) against the experimental ABL height measurements. Two of these models encompass the effect of the free-atmosphere stability, quantified by the Brunt–Väisälä frequency. The latter is then validated against the analogous estimates obtained from simultaneous and co-located radiosonde profiles of potential temperature. Finally, leveraging the year-long span of the present measurements, the variability of the ABL height model parameters is linked to the presence of synoptic timescales driving the flow throughout the year.

This paper is organized as follows: in Sec. II, the experimental campaign, LiDAR scanning strategy, and quality control processes are detailed. In Sec. III, both the predictive and the diagnostic ABL height models used in this work are introduced. Results are presented in Sec. IV, and conclusions are discussed in Sec. V.

II. EXPERIMENTAL DATA COLLECTION

A. Experimental site, instrumentation, and scanning strategy

The data presented in this work are collected at the AWAKEN C1a site located midway between the King Plains and Armadillo Flats wind farms (cf. with Fig. 1), mainly featuring north-south wind conditions.[11,50–52] Among the instruments deployed at site C1a by different research teams, this study focuses on the data collected by two sensing instruments, namely, one Streamline XR scanning pulsed Doppler LiDAR (manufactured by Halo Photonics) and one surface flux station, both owned by The University of Texas at Dallas and deployed from October 4, 2022, to October 14, 2023. The surface flux station is equipped with two CSAT3-3D sonic anemometers (manufactured by Campbell Scientific Inc.) mounted at 2 m height along the prevailing wind direction (north–south) probing the three-dimensional wind vector and temperature within a measurement volume of the order of 0.1 m and sampling rate of 20 Hz, thus fully resolving the shear and buoyancy turbulent motions close to the ground.

In order to probe vertical distributions of velocity variance ($\overline{w'w'}$) and time-averaged signal-to-noise ratio (SNR), which represents two quantities typically utilized to estimate the ABL height,[32,53] the Streamline XR LiDAR performed 10-min-long vertical-staring measurements with 48 m range gate and 2 Hz sampling rate. The measurement range spans from 120 m above the ground (end of the LiDAR's blind zone) up to 5976 m through 123 non-overlapping gates. In total,
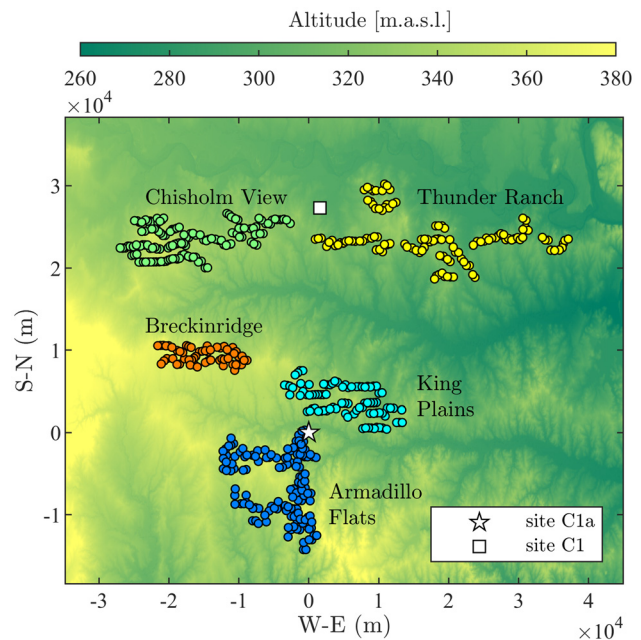

FIG. 1. Elevation map of the AWAKEN site (source: United States Geological Survey), the wind farms (colored circles) investigated, the deployment location of the LiDAR (white star), and the ARM SGP C1 site where radiosondes were launched from (white square). The axes reference the C1a site location.

6734 vertical stare measurements (each of them with a 10-min measurement period) were collected. For further details about the LiDAR's working principle, as well as the internal laser architecture, the reader is referred to the study of Wu et al.[54]

As detailed in Sec. III, one of the fundamental scaling parameters governing the ABL evolution is the mean potential temperature gradient in the free atmosphere,[2] which is quantified by the Brunt–Väisälä frequency. The latter will be estimated from the ABL height models calibrated onto the LiDAR data (see Sec. IV B). To validate the best-fitted values of the Brunt–Väisälä frequency, the radiosonde data collected by the DOE Atmospheric Radiation Measurement (ARM) at the SGP central facility (site C1, nearly 30 km north of site C1a, reported in Fig. 1 with white square symbol)[55] are included in the present analysis. Each radiosonde returns instantaneous profiles of dry air temperature and pressure sampled with variable vertical resolution (0.1–40 m), thereby allowing for the calculation of the instantaneous profile of potential temperature from the ground proximity (≈ 300 m) to well above the ABL height (≥ 5000 m). Five different hours across the day are considered in this study when radiosonde data are available: 02:00 UTC (21:00 local time), 05:00 UTC (00:00 local time), 11:00 UTC (06:00 local time), 17:00 UTC (12:00 local time), and 23:00 UTC (18:00 local time). Each launch is repeated across different days within the period October 4, 2022– October 14, 2023, in order to provide statistical significance to the retrieved quantities (50, 171, 188, 160, and 208 launches are done at each mentioned hour, respectively). For each considered time, the instantaneous vertical profiles of potential temperature are ensemble averaged over a common vertical coordinate spanning from 300 to 3000 m with vertical resolution of 50 m, and eventually utilized to calculate the vertical profiles of the Brunt–Väisälä frequency [see Eq. (5)].

B. Quality control of the sonic data

Before moving forward with the quantification of the ABL height, the sonic anemometer data are analyzed through a quality control process to obtain statistically accurate turbulence estimates near the ground. For each overlapping time period with the LiDAR, the 3D sonic velocity vector is first aligned in the streamwise, transverse, and vertical directions (x, y, z) following the algorithm of Wilczak et al.[56] (the x-direction is associated with the mean wind direction evaluated over the whole 10-min period). The velocity components are hereafter indicated as (u, v, w) along (x, y, z), respectively. Then, the data collected from the upwind sonic anemometer, which are deemed not obstructed by the wake generated by the anemometer supporting structure, are used to retrieve friction velocity (u_τ) and Obukhov length (L). In this work, the friction velocity is calculated via the eddy covariance method[1]

$$u_\tau = \left(\overline{u'w'}^2 + \overline{v'w'}^2\right)^{0.25}, \tag{1}$$

where the prime index indicates zero-mean turbulent velocity fluctuations. The Obukhov length is defined as

$$L = -\frac{u_\tau^3 \Theta}{g\kappa \overline{w'\theta'}}, \tag{2}$$

where Θ is the mean virtual potential temperature, $g = 9.81$ ms^{-2} is gravity acceleration, $\kappa = 0.41$ is the Von Kármán constant, and $\overline{w'\theta'}$ is the vertical heat flux (θ' being the zero-mean temperature fluctuation).

To obtain reliable estimates of these two statistical quantities, the following requirements are enforced:

1. The statistical uncertainty of u_τ (Δu_τ) must be lower than 20% of the expected value [calculated via Eq. (1)].
2. Krishnamurthy et al.[11] have shown that hourly averaged values of friction velocity collected at the ARM SGP C1 site are statistically bounded within 0.25 and 0.45 ms^{-1} throughout the day. Thus, only friction velocity values smaller than 1ms^{-1} are considered in the rest of this study.
3. The statistical uncertainty of L (ΔL) must be lower than 50% of the expected value [calculated via Eq. (2)].

The present quality control of 3D sonic anemometer data is assessed against the Monin–Obukhov similarity theory; furthermore, details are reported in Appendix B. It is noteworthy that the statistical uncertainties of both u_τ and L are calculated via bootstrap algorithm over 100 subset periods containing 500 points each[57] using Eqs. (1) and (2), respectively. As expected, the enforcement of these requirements reduces the data availability. The relative percentage of data reduction introduced by each criterion is reported in Fig. 2(a) with black bars, while the cumulative percentage of data rejection is reported in Fig. 2(b). Here, it is observed that the largest source of data rejection (34.2%) is given by the unavailability of the sonic anemometer data, while the aforementioned criteria cause relatively small percentage of data reduction (9.9% and 13%, respectively). Eventually, of the 6734 LiDAR and sonic datasets, 2892 (42.9%) are left for further analysis after the quality control of the sonic anemometer data.

C. Quality control of LiDAR data

Focusing on the Streamline XR datasets, only LiDAR data taken simultaneously with the quality-controlled sonic anemometer data are
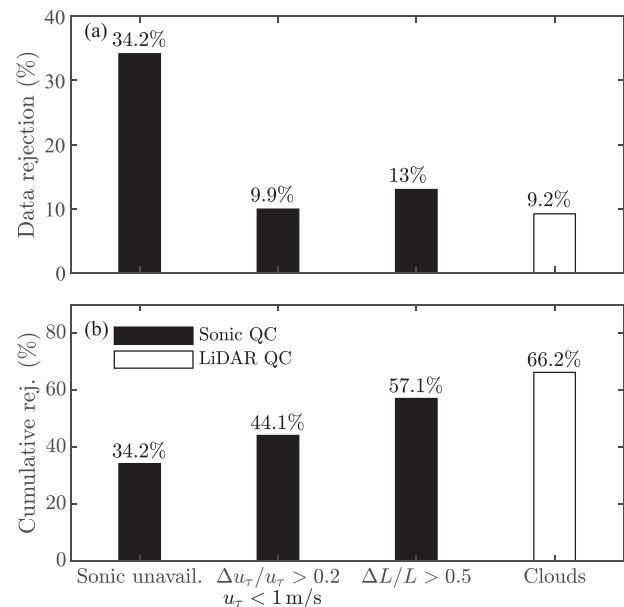
FIG. 2. Data rejection due to quality control (QC) procedure. (a) Percentage of data rejection caused by each criterion. (b) Cumulative data rejection rate.

considered for further analysis. Among them, those featuring cloudy conditions are removed. This requirement is checked based on the variance of the attenuated backscatter (β_{att}) at each height [$\sigma_\beta(z)$]. In particular, datasets showing $\sigma_\beta \geq 10^{-8} \text{m}^{-2}\text{srad}^{-2}$ at any measured height are considered to be affected by the presence of clouds are discarded from further analysis. The attenuated backscatter is automatically calculated by the Streamline XR LiDAR model as the product of a calibration curve [$C_\beta(z)$] and the range-corrected SNR ($z^2\text{SNR}$):[58] $\beta_{\text{att}}(z,t) = C_\beta(z)z^2\text{SNR}(z,t)$. Of the 2892 selected LiDAR datasets, 2274 (representing the 33.8% of the 6734 datasets initially available) are retained after the sonic and LiDAR quality control process (cf. with Fig. 2), which are subsequently utilized to estimate the ABL height.

For all the cloud-free LiDAR datasets, the dynamic filtering algorithm developed by Beck and Kühn[59] is implemented to remove instantaneous outliers present in the vertical velocity time series, which could bias the quantification of this statistical moment. Specifically, for each time record at each height, instantaneous samples featuring either vertical velocity fluctuations outside of the interval ± 3 m/s or SNR outside of [$-20, 0$] dB are marked as outliers and removed. As shown in Sec. III B, the velocity variance profiles are utilized to estimate the ABL height only during nighttime hours, i.e., when the thermal conditions are mostly stable. Thus, although the choice of limiting the vertical velocity fluctuations to ± 3 m/s might seem too restrictive for daytime convective conditions, this threshold does not influence the quantification of ABL height during nighttime, when the vertical velocity fluctuations are typically much less than ± 3 m/s. Subsequent to the choice of thresholds, for each instantaneous realization, a normalized bivariate probability density function of w and SNR is calculated considering all the samples within 150 s. All the normalized (w, SNR) samples with occurrence less than 0.1% are considered outliers, and the respective instantaneous velocity record is removed from the time series. Notably, this algorithm is implemented only to remove the incorrect estimates of vertical velocity, whereas no action is done on the SNR.

III. ATMOSPHERIC BOUNDARY LAYER HEIGHT QUANTIFICATION

A. Predictive models for the atmospheric boundary layer height

As mentioned in the Introduction, several models have been developed to predict the ABL height involving both near-ground shear and thermal conditions and the free troposphere stability. In this subsection, five ABL height models available in the literature are introduced (one related to convective thermal conditions and four related to stable conditions), which will be subsequently validated against the ABL height estimates (Sec. IV B). The advantages and limitations of each of these models are discussed, as is the physical meaning of the free parameters utilized by the models.

1. The Rossby and Montgomery model

The earliest parameterization of the ABL height was proposed by Rossby and Montgomery,[60] where the ABL height for neutrally stratified flows is estimated from the Reynolds-averaged momentum balance between geostrophic wind and surface drag:[15]

$$\frac{z_i}{L} = C\mu, \tag{3}$$

where

$$\mu = \frac{u_\tau}{fL} \tag{4}$$

is a parameter accounting for the Earth's rotation and thermal stability (see, e.g., Ref. 61) ($f = 8.62 \times 10^{-5}$ Hz is the Coriolis frequency), and $C \approx 0.1$–0.5 is a constant introduced in Eq. (3) to empirically account for non-neutral conditions.

2. The Zilitinkevich and Mironov model

The Rossby and Montgomery[60] formulation may be used for non-neutral conditions by changing the value of the constant C. However, a precise modeling of the thermal buoyancy and free-flow stability is absent in Eq. (3). These two effects are typically quantified by the Obukhov length (L) and the Brunt–Väisälä frequency (N), respectively. The latter is defined as

$$N = \left(\frac{g}{\Theta}\frac{d\Theta}{dz}\right)^{0.5}. \tag{5}$$

Physically, the Brunt–Väisälä frequency represents the frequency at which a parcel oscillates around its equilibrium height under a stably stratified mean potential temperature profile, and it is typically of the order of 0.01 s^{-1}. This quantity will be estimated both directly from the radiosonde measurements of potential temperature and indirectly from the best-fit of those ABL height models involving N in their parameterization of the ABL height.

For a stably stratified flow, Zilitinkevich and Mironov[16] provided a comprehensive multi-limit formulation derived from the turbulent kinetic energy equation under several heuristic assumptions (i.e., steady-state flow, logarithmic mean velocity profile, first-order approximation of resistance law and heat flux, and energy-transferring gravity waves at the boundary between ABL and residual layer)

$$\left(\frac{fz_i}{C_n u_\tau}\right)^2 + \frac{z_i}{C_s L} + \frac{z_i N}{C_i u_\tau} + \frac{z_i f^{0.5}}{C_{sr}(u_\tau L)^{0.5}} + \frac{z_i (Nf)^{0.5}}{C_{ir} u_\tau} = 1, \tag{6}$$

where $C_n = 0.5$, $C_s = 10$, $C_i = 20$, $C_{sr} = 1.0$, and $C_{ir} = 1.7$ are empirically determined constants. In Eq. (6), the first three terms of the left-hand side are related to the isolated effects of Earth's rotation, thermal stability, and free-flow stratification, respectively, while the fourth term accounts for the combined effects of Earth's rotation and thermal stability, and the fifth term is related to the combined effect of Earth's rotation and background stratification. Thus, Eq. (6) may be used to predict z_i under the simultaneous presence of all the driving mechanisms during stable conditions.

3. The Steeneveld model

The model of Zilitinkevich and Mironov[16] relies on a large number of assumptions, which are rarely verified in a real flow scenario all together. Indeed, Steeneveld et al.[18] observed a systematic underestimation of z_i when obtained from Eq. (6) as compared to the experimental reference under a broad range of free-flow stratification. To address this issue, the authors proposed a new parameterization of z_i solely based on dimensional considerations

$$\frac{z_i}{L} = \left(\frac{\left|\frac{g}{\Theta}\overline{w'\theta'}\right|}{\alpha u_\tau f N L}\right)^{\frac{1}{C_1 - k\left(\frac{N}{f}\right)}}, \tag{7}$$

where $\alpha = 3$, $C_1 = 1.8$, and $k = 10^{-3}$ are empirical constants.[18] The main advantage of Eq. (7) with respect to Eq. (6) is that the empirical exponent on the right-hand side of Eq. (7), typically greater than 1, greatly improves the agreement with the data.[18] In the present work, Eq. (7) will be calibrated on the ABL height values retrieved by the LiDAR by means of a least squares best-fit algorithm. Lacking a direct quantification of the Brunt–Väisälä frequency to be used in Eq. (7) (which would require temperature measurements up to the ABL height), in this study N/f will be fitted onto the experimental data alongside α letting $C_1 = 1.8$ as a fixed parameter. Eventually, the fitted value of N/f will be validated against the vertical profiles of Brunt–Väisälä frequency quantified by the radiosonde measurements. The reason why C_1 is fixed and α is left as a free parameter is that, for any fixed value of N/f, any offset of the z_i/L distribution results in the increase or decrease in α, whereas the variability of C_1 is less straightforward to interpret. This feature will be useful in Sec. IV C where α will be calibrated over seasonal subsets of the AWAKEN dataset to relate the variability of α to the seasonal trends. Finally, in Eq. (7), the quantities Θ, $\overline{w'\theta'}$, u_τ, and L are calculated from 3D sonic measurements, while z_i is estimated from LiDAR data.

The constant k is empirically quantified by Steeneveld et al.,[18] plotting the left-hand side of Eq. (7) vs the argument in parenthesis for different intervals of N/f. For the present study, it is assumed that N/f in stable conditions is of the same order of magnitude as in convective conditions ($N/f \approx 100$ at the SGP sites[62,63]). The constant k is iteratively chosen based on this assumption; eventually, a value of $k = 4 \times 10^{-3}$ is set in the remainder of this work.

It is noteworthy that all the best-fitted values mentioned in this work have been obtained in Matlab through the nonlinear least squares optimization method implementing a Trust-Region algorithm.[64] The only constraint imposed on the optimization problem is that all the ABL model parameters must be greater than 0. The minimum of the cost function is then sought iteratively through the minimization of the second-order local approximation of the cost function, where the Jacobian and Hessian matrices are evaluated trough second-order central finite difference schemes. The iterative search is stopped when one of the following criteria is verified: a maximum of 400 iterations is reached; the cost function changes by a value less than 10^{-6}; the norm of the incremental step is less than 10^{-6}. Notably, for all the tested cases, the iterative algorithm stopped because the cost function increment was lower than 10^{-6}.

4. The Joffre model

Another important parameterization of the stable ABL height is provided by Joffre et al.,[13] who assessed the multi-limit formulation of Zilitinkevich and Mironov[16] over a relatively wide range of μ (1–100). Similar to Steeneveld et al.[18] and Joffre et al.[13] also pointed out the underestimation of z_i done by Eq. (6) for strongly stable flows ($\mu > 10$). By contrast, for moderately stable conditions ($1 \leq \mu \leq 10$), the authors proposed a quasi-linear empirical relationship to estimate z_i:

$$\frac{z_i}{L} = 0.082\mu^{1.07}. \tag{8}$$

As shown in Sec. IV, the stability range covered by the current AWAKEN database spans from $\mu \approx 1$ to 10^3. To address this point, we propose a generalization of Eq. (8) as follows:

$$\frac{z_i}{L} = C\mu(1 + \beta\mu^\gamma), \tag{9}$$

where β, γ are positive constants to be calibrated on the data, and C is the same constant of Eq. (3). Indeed, as $\mu \to 0$ (i.e., conventionally neutral conditions), the term in parenthesis goes to 1 and the formulation of Rossby and Montgomery[60] is retrieved [cf. with Eq. (3)]. Thus, we expect Eq. (9) to cover the whole range of stability, from neutral to strongly stable. Analogous to α in Eq. (7), the constant C accounts for any shift of the μ vs z_i/L distribution along the ordinate axis. Therefore, this constant will be calibrated in Sec. IV C by means of a least squares fit to capture any synoptic variability in the stable ABL height. In Eqs. (8) and (9), the parameter μ is calculated based on 3D sonic data [cf. with Eq. (4)], while z_i is retrieved from LiDAR measurements.

5. The Kitaigorodskii model

Focusing on convective conditions, the temporal growth rate of z_i due to buoyancy- and shear-produced turbulence must be taken into account solving a time-dependent governing equation, typically represented by the turbulent kinetic energy (TKE) equation.[65] In this scenario, Kitaigorodskii and Joffre[12] provided the following parameterization:

$$\frac{z_i}{L} = \frac{1 + \left[1 + 4a'm''\left(\dfrac{u_\tau}{LN}\right)^{-2}\right]^{0.5}}{2a'\left(\dfrac{u_\tau}{LN}\right)^{-2}}, \tag{10}$$

where $a' = 0.1 - 0.3$ and $m'' \approx 6$. Equation (10) will be calibrated on the AWAKEN data in convective conditions letting N and m'' be free parameters and keeping $a' = 0.2$ fixed. Analogous to α in Eq. (7), any increase (decrease) of m'' is caused by upward (downward) shifts of the μ-vs-z_i/L distribution along the ordinate axis. Thus, m'' is expected to model the synoptic variability within the convective ABL height estimates (cf. with Sec. IV C). In Eq. (10), u_τ and L are obtained from 3D sonic measurements, while z_i is retrieved from LiDAR measurements.

B. Algorithms to estimate the atmospheric boundary layer height based on LiDAR data

In the context of the daytime convective ABL, the vertically staring Streamline XR Doppler LiDAR is utilized during the AWAKEN campaign to probe vertical turbulent motion. The time-vs-height quantification of the attenuated backscatter (β_{att}), assumed as an indirect estimate of the local aerosol concentration,[66] is provided by the LiDAR as well. The latter is a compelling quantity when it comes to estimating the convective ABL height, since the daytime turbulent mixing induces an almost uniform aerosol concentration throughout the mixed layer, whereas the entrainment zone aloft is characterized by a sharp decrease, eventually leading to the low aerosol concentration in the free atmosphere. Thus, the height associated with a rapid decrease in aerosol concentration (or, equivalently, β_{att}) represents a physically sound estimate of the ABL height in the presence of a well-established mixed layer.[32,67] It is noteworthy that, for the Streamline XR LiDAR used in the present work, the attenuated backscatter is calculated as[58] $\beta_{att}(z, t) = C_\beta(z)z^2\text{SNR}(z, t)$, where $C_\beta(z) > 0$ is a calibration curve

<div style="text-align: right">28 October 2024 18:15:46</div>

provided by the manufacturer and accounting for the laser focus function. Since the latter may drift from the calibration conditions in time, a recalibration of $C_\beta(z)$ against simultaneous and independent measurements of β_{att} is required. Lacking this possibility, for the present experiment, we assume the range-corrected time-averaged SNR (z^2SNR) as an indicator of the local aerosol properties (as previously done, e.g., by Kong and Yi,[32] Menut et al.,[33] and Toledo et al.[68]).

Several diagnostic methods have been defined to capture rapid changes in the aerosol properties, for instance, based on the vertical evolution of the mean attenuated backscatter[27] as well as the maximum attenuated backscatter variance,[33] particle depolarization, and LiDAR ratio.[32] Regardless of the particular quantity used, one method largely applied to individual sharp transitions of the aerosol properties

is the wavelet covariance transform[28,30,42,67,69] (WCT), which is used in this work to estimate the ABL height from LiDAR data during daytime. The details of this method are provided in Appendix A.

The WCT method, however, has two main limitations. First, it may lead to incorrect ABL estimates in the presence of multilayered aerosol structures. Second, a mixed layer must be well established in the ABL to maintain high and uniform aerosol concentrations. This is not the case during nighttime and early morning conditions, when the ABL is characterized by a thin layer of shear-generated turbulence close to the ground and a residual layer aloft. To address the first point, a careful inspection of all the datasets is conducted based on the visualization of the time-vs-height plots of vertical velocity and range-corrected SNR; examples of these plots are reported in Figs. 3(a), 3(b),
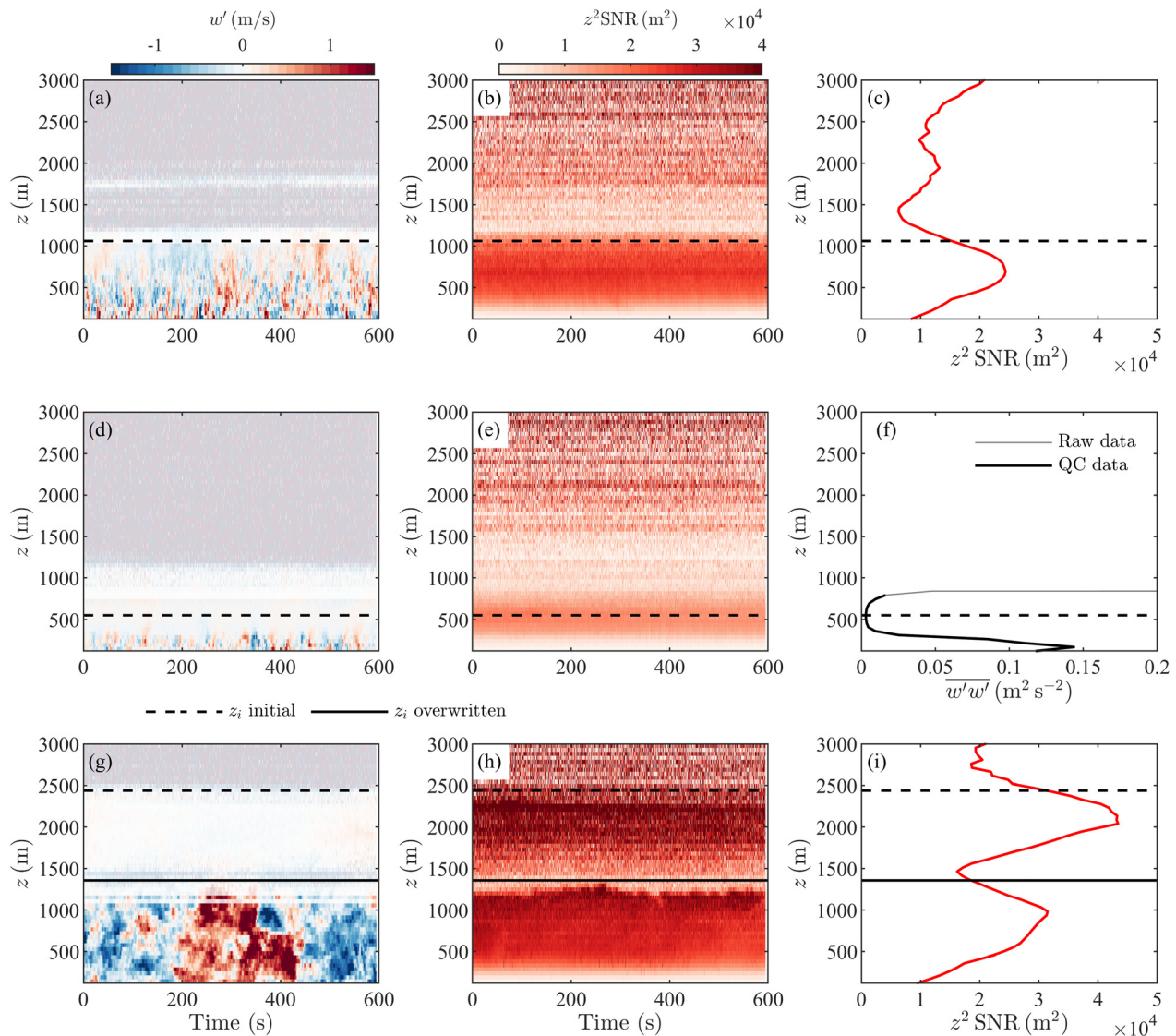

FIG. 3. Example of ABL height quantification (dashed and continuous line) for convective (a)–(c) and stable (d)–(f) conditions. Panels (g)–(i) show an example of manually overwritten ABL height in the presence of a multilayer aerosol structure. Plots (a), (d), and (g) show the color contours of vertical velocity fluctuation; plots (b), (e), and (h) show the range-corrected SNR, and plots (c), (f), and (i) show the vertical distribution of the statistical quantity utilized for the ABL height estimation.

3(d), 3(e), 3(g), and 3(h) for quality-controlled datasets. In regard to the second point, the WCT method is used only with datasets collected after 16:00 UTC time (corresponding to 11:00 local time), where a convective mixing is assumed to be present; this choice of threshold will be further discussed in Sec. IV A.

When the dataset does not show a sufficiently high positive buoyancy production (typically before 16:00 UTC), the vertical distribution of range-corrected SNR is not a reliable source to estimate the ABL height. However, shear-induced turbulence is still expected to be generated at the ground and rapidly decrease moving upward. In the absence of non-canonical stable ABL events (such as gravity waves, bores, and shear instabilities), literature results have identified the ABL height in several ways, such as the height at which the streamwise velocity variance reaches a minimum[37] as well as the height at which the variance of vertical velocity is less than a certain percentage of its value at the ground.[22] In this work, we assume the local minimum of vertical velocity variance (after the quality control procedure described in Sec. II C) as the best estimator of the ABL height in stable conditions. An example of this method is visualized in Fig. 3(f).

After estimating the ABL height for all the available datasets, a further quality check is implemented to avoid the presence of non-physical estimates in the database. These outliers are associated with extreme over- or underestimation of the ABL height; thus, the z_i estimates are grouped into non-overlapping hour-long bins and, for each of them, datasets featuring ABL height less than the 5th percentile or greater than the 95th percentile are further investigated. In particular, the ABL height is manually overwritten based on the visual inspection of time-vs-height plots of vertical velocity and range-corrected SNR. An example of this procedure is reported in Figs. 3(g)–3(i), where two layers of high aerosol concentration (roughly located at 1400 and 2200 m, respectively) are evidenced in the range-corrected SNR pattern [Fig. 3(h)]. The WCT initially quantifies the ABL height as 2426 m (dashed line); however, the visual inspection of the vertical velocity pattern [Fig. 3(g)] shows negligible turbulent fluctuations above 1357 m (continuous line). Thus, the latter is assumed as the new ABL height value for the considered dataset. In total, 155 ABL height values (6.8%) are manually checked.

IV. RESULTS

A. Assessment of the daily cycle of atmospheric boundary layer height

After estimating the ABL height through the above-mentioned diagnostic methods, the calculated z_i values are used to evaluate the daily cycle of ABL height. The latter is reported in Fig. 4(a) overlapped to the daily cycle of vertical velocity variance. The analogy between the distributions of z_i and $\overline{w'w'}$ confirms that the primary mechanism governing the ABL evolution at the tested site is the thermal stability. From Fig. 4(a), the vertical velocity variance reaches its maximum between 16:00 and midnight (UTC time) due to the onset of a positive buoyancy flux which, in turn, enhances the aerosol mixing within the ABL. As anticipated in Sec. III B, the WCT method can only be applied in the presence of significant turbulent mixing; thus, it is utilized only for datasets collected between 16:00 and midnight, whereas the minimum vertical velocity variance method is used for the remaining data. This time cutoff is highlighted in Fig. 4(a) with a vertical dashed line.

The ABL height can be further assessed comparing the current daily cycle against the analogous estimates obtained by Krishnamurthy et al.,[11] who used a machine learning algorithm on a years-long scanning LiDAR database collected at the ARM SGP C1 site ($\approx$ 30 km north of the C1a site) via vertical-staring scans. The result, reported in Fig. 4(b), demonstrates strong quantitative agreement between the current daily cycle and the literature result, both in the hourly averaged ABL height values (black symbols) and in the standard deviation (vertical uncertainty interval). The temporal oscillation of the current daily cycle is deemed to be caused by the relatively short sampling period (10 min) of each vertical scan.

B. Stability dependence of the atmospheric boundary layer height

After comparing the current ABL height estimates against previous results, the dependence of z_i on the thermal conditions is investigated by plotting the stability parameter z_i/L against μ (Fig. 5) distinguishing between convective [Fig. 5(a)] and stable [Fig. 5(b)] conditions. To facilitate the visual comparison between the data and
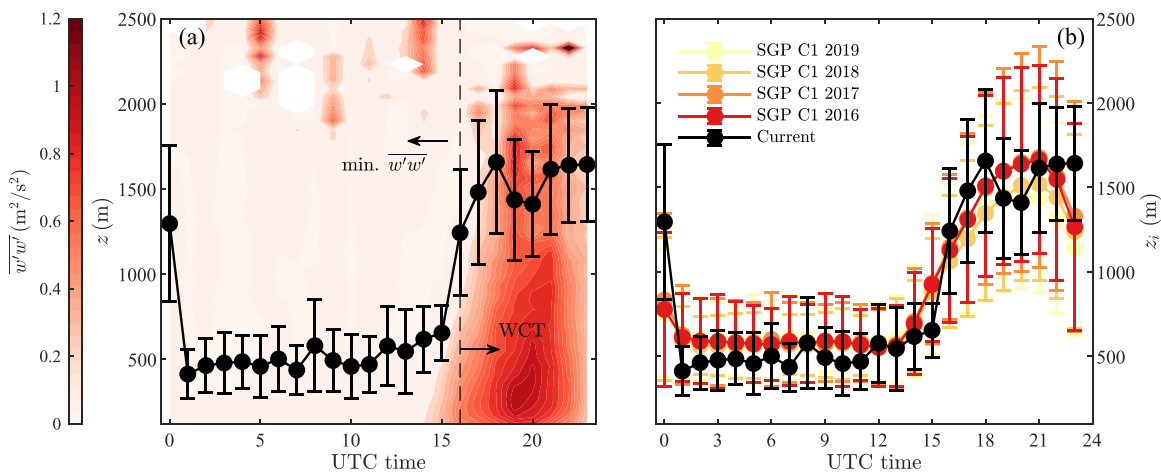

FIG. 4. (a) Daily cycle of vertical velocity variance ($\overline{w'w'}$) and hourly averaged ABL height (indicated with black symbols; uncertainty intervals report one standard deviation around the mean). (b) Daily cycle of hourly averaged z_i compared with previous results of Krishnamurthy et al.[11] at the ARM SGP C1 site.
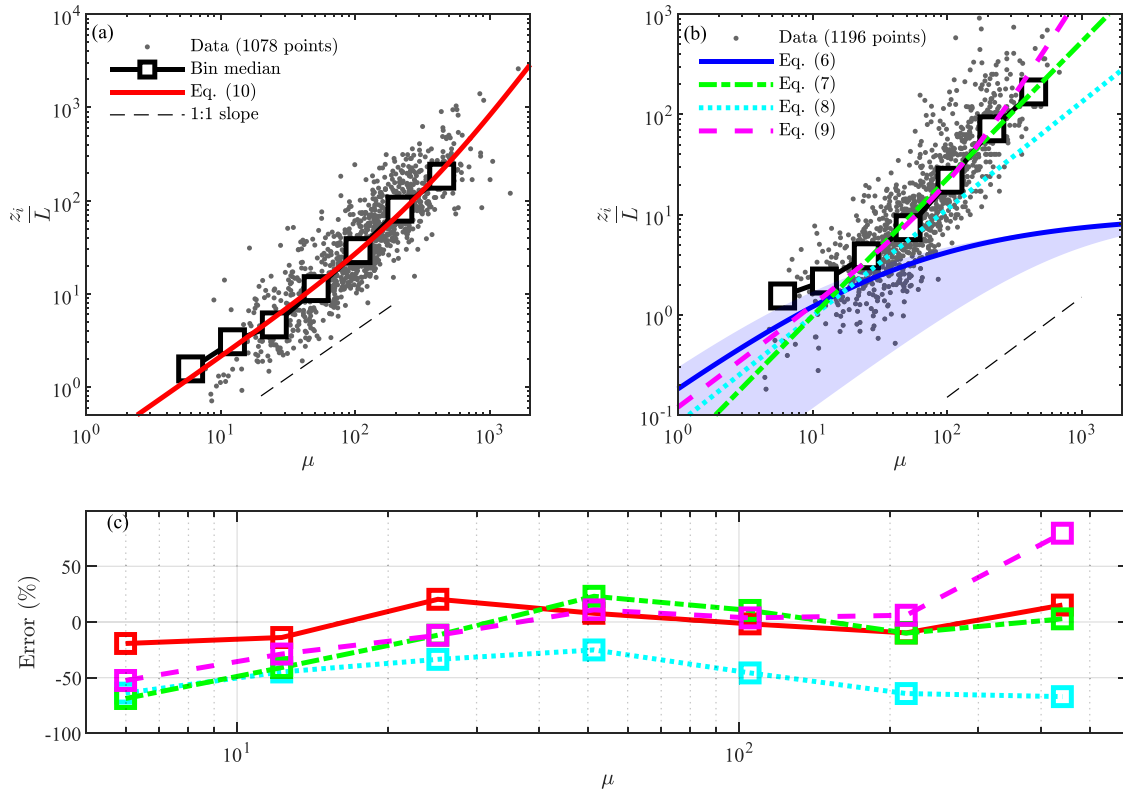
28 October 2024 18:15:46

FIG. 5. Stability dependence of the ABL height on the parameter μ for convective (a) and stable (b) conditions. In (a), the red line reports the calibrated model of Kitaigorodskii and Joffre[12] In (b), the blue, cyan, and green lines report the models of Zilitinkevich and Mironov[16] (blue region corresponds to $1 \leq N/f \leq 10^3$), Joffre et al.,[13] and Steeneveld et al.,[18] respectively, while the magenta line reports the calibration of Eq. (9). (c) Percentage error between the bin-averaged experimental value and the model prediction; the lines are colored according to the legend of plots (a) and (b).

the models, as well as the departure of the data from the $1:1$ linear trend [dashed lines in Figs. 5(a) and 5(b)], bin-averaged values of z_i/L (white filled squares) are overlapped on the data.

1. Convective conditions

Focusing on convective conditions first [Fig. 5(a)], strong agreement is found between the data and the calibrated model of Kitaigorodskii and Joffre[12] [Eq. (10)], the latter fitted over 1078 data points. The relative error distribution between the bin-averaged data values and the Kitaigorodskii and Joffre[12] model prediction, reported in Fig. 5(c) with red symbols and continuous line, indicates percentage errors between -19% and 15%. However, the root-mean-square error (RMSE) and mean absolute error (MAE) between the ABL height evaluated experimentally and predicted by the model are quite large (798 and 585 m, respectively, as reported in Table I); these large values are deemed to be caused both by the large variability of the convective ABL height values [visualized by the large scattering of data points in Fig. 5(a) and by the large uncertainty intervals in Fig. 4(b)] and by the lack of direct quantification of the Brunt–Väisälä frequency simultaneous to each ABL height estimate.

The calibrated model parameters (m'', N/f) are reported in Table I as well. The fitted value of m'' (9.31) is of the same order of magnitude as the one proposed by Kitaigorodskii and Joffre[12] ($m'' = 6$), although

larger. A possible justification of this discrepancy may be found in the synoptic variability of the ABL height across different seasons,[11] which will be investigated in Sec. IV C. Finally, the calibrated value of $N/f = 90$ agrees with previous estimates of the nondimensional Brunt–Väisälä frequency ($N/f \approx 10^2$) at SGP latitudes.[62] Furthermore, the

TABLE I. Calibration of different ABL height models. The quantities in parenthesis report the 95% confidence interval. The last two columns report the root-mean-squared error (RMSE) and the mean absolute error (MAE) between the ABL height quantified by the LiDAR and each model's prediction, respectively.

Reference	Eq. #	Fit parameters	z_i RMSE (m)	z_i MAE (m)
Ref. 12	10	$m'' = 9.31\,(\pm 1.42)$ $N/f = 90\,(\pm 8)\,(L < 0)$	798	585
Ref. 18	7	$\alpha = 3.0\,(\pm 0.2)$ $N/f = 85\,(\pm 13)\,(L > 0)$	474	281
Proposed model	9	$C = 0.119\,(\pm 0.017)$ $\beta = 2.7 \times 10^{-3}\,(\pm 4.6 \times 10^{-3})$ $\gamma = 1.22\,(\pm 0.28)$	484	288

vertical profiles of the Brunt–Väisälä frequency obtained from the radiosonde data from site C1 are reported in Fig. 6(f) for each considered hour when launches are available. The vertical profiles of mean potential temperature utilized to calculate N/f are reported in Figs. 6 (a)–6(e) for each considered launch time. The N/f interval evaluated from radiosondes during daytime convective conditions [launches at 17:00 and 23:00 UTC, reported with red and magenta lines in Fig. 6(f)] spans from 50 to 200 at different heights, thus in good agreement with the value retrieved from the Kitaigorodskii and Joffre[12] model ($N/f = 90$). In conclusion, the current estimates of the convective ABL height from AWAKEN data lead to an overall good level of agreement with the theoretical prediction of Kitaigorodskii and Joffre,[12] although this model is not able to completely capture the ABL height variability in convective conditions.

2. Stable conditions

For stable conditions [Fig. 5(b)], we first observe an increase in z_i/L with slope greater than 1 increasing the stability ($\mu \gtrsim 10^2$), consistently with previous results.[13,18] Thus, the model of Zilitinkevich and Mironov[16] [reported in Fig. 5(b) with blue line], which predicts a less-than-linear power law for very stable conditions, largely underestimates the ABL height. Notably, this outcome does not depend on the uncertainty on the Brunt–Väisälä frequency as evidenced from the

blue shaded area in Fig. 5(b), which is obtained solving Eq. (6) letting $1 \leq N/f \leq 10^3$. Similarly, the parameterization of Joffre et al.[13] [Eq. (8), reported in Fig. 5(b) with cyan line], although it models the monotonic increase in z_i/L with μ, underestimates the stability-corrected ABL height by 26% or more as evidenced by the percentage error distribution in Fig. 5(c) (cyan symbols).

Better agreement is found calibrating the model of Steeneveld et al.[18] [Eq. (7), green line in Fig. 5(b)], which leads to large percentage errors (-69% to $+51\%$) for neutral to moderately stable conditions ($\mu \leq 50$) followed by smaller values ($< 10\%$) for the rest of the stability interval [cf. with Fig. 5(c)]. This feature indicates that the model of Steeneveld et al.[18] is better suited for strongly stable conditions. The overall fitted value of α (3.0, cf. with Table I), however, is in excellent agreement with the one proposed by Steeneveld et al.[18] ($\alpha = 3$), and the obtained value of N/f (85 ± 13) is in good agreement with previous estimates in the SGP area during nighttime conditions ($N = 0.01$ Hz, corresponding to $N/f \approx 116$).[63] Similarly, the N/f interval in stable conditions retrieved from the radiosonde data ($100 \leq N/f \leq 300$ indicated by the cyan line in Fig. 6(f), related to radiosonde launches done at 02:00 UTC) agrees well with the value calibrated from the model of Steeneveld et al.[18]

Finally, the currently proposed parameterization of the stable ABL height [Eq. (9)] is calibrated onto the experimental data and reported in Fig. 5(b) with the magenta line. It is noticed that, among
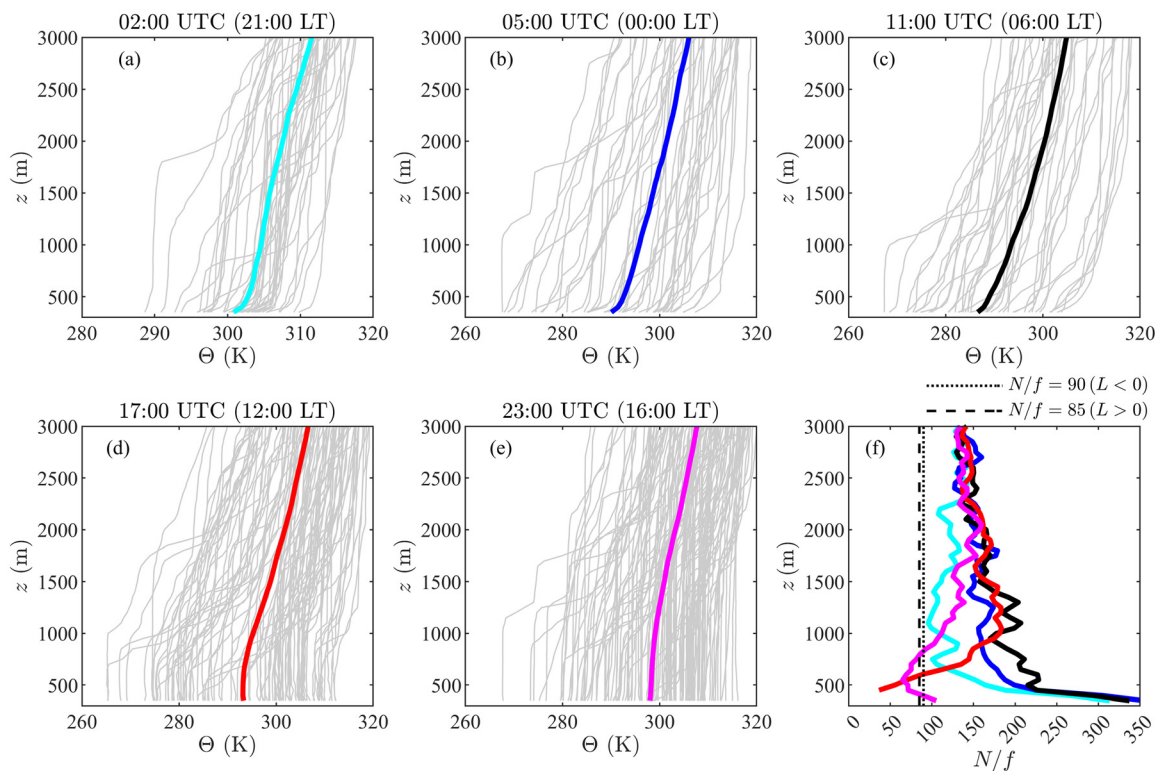

FIG. 6. Mean potential temperature profiles retrieved from radiosonde measurements. Plots (a)–(e) report the instantaneous potential temperature in gray and the average as the colored line; the title reports the launch time in UTC and local time (LT) format. Plot (f) reports the vertical profiles of the Brunt–Väisälä frequency [cf. with Eq. (5)] divided by the Coriolis frequency; the line colors are the same as reported in plots (a)–(e). The N/f values calibrated on the ABL height from LiDAR measurements are reported in dotted and dashed lines for convective and stable conditions, respectively.

the models introduced to parameterize the stable ABL height, Eq. (9) leads to the smallest percentage error distribution across μ, mainly due to the fact that it relies on the largest number of free parameters. The value of the constant C (0.119, cf. with Table I), quantifying the linear growth rate of the ABL for weak stability, is in good agreement with the order of magnitude of C in Eq. (3) for stable conditions ($C \approx 0.12$) found in the literature.[70] This confirms the initial hypothesis that Eq. (9) may be seen as a generalization of the geostrophic drag law valid for the entire stability range. The fitted value of $\beta = (2.7 \pm 4.6) \times 10^{-3}$ is uncertain due to the large scattering of ABL height values across the stability range. This is related to the difficulty of estimating the ABL height while lacking a well-defined boundary between turbulent and non-turbulent portions of the atmosphere for nighttime conditions. Finally, the value $\gamma = 1.22$ captures the growth of z_i/L for strongly stable conditions. It is noteworthy that Eq. (9) can be approximated by $z_i/L \approx C\beta\mu^{\gamma+1}$ as $\mu \gg 1$. Given the current value of γ, we obtain the following expression for strongly stable conditions: $z_i/L \propto \mu^{2.22}$. Joffre et al.[13] estimated a growth rate proportional to $\mu^{1.5}$ for $10 \leq \mu \leq 100$. The faster growth of z_i/L currently found is thought to be a consequence of the larger extension of the current stability range ($1 \leq \mu \leq 10^3$) over which the behavior of z_i/L is modeled.

For stable conditions, the RMSE (484 and 474 m) and MAE (288 and 281 m) values between the experimental ABL height values and the model predictions are large (see Table I), although lower than what was found for convective conditions. It is noticed that the models of Eqs. (7) and (9) lead to similar values of RMSE and MAE. This feature, together with the agreement between each model's constants and the literature values, leads to the conclusion that the discrepancy between the experimental values and the prediction is due to the uncertainties in the experimental quantification of the ABL height rather than a

limitation of the models to capture the flow physics. Thus, the current stable ABL height dataset is in good agreement with the stability trend predicted by the models, even though the uncertainty associated with the experimental ABL height estimates leads to significant mean error values with respect to the models' predictions.

C. Seasonal variability of the parameters

The availability of ABL height estimates over one year is now leveraged to quantify the effect of seasonal timescales on the ABL height model parameters. To this aim, the data are binned into four subsets spanning three months each, namely, December–January–February (DJF), March–April–May (MAM), June–July–August (JJA), and September–October–November (SON). The daily cycles of z_i and vertical velocity variance are reported in Fig. 7 for each data bin. Focusing on daytime convective conditions (i.e., after 16:00 UTC, reported with vertical dashed line), smaller velocity variance is observed for the period DJF with respect to the baseline daily cycle [Fig. 7(a)] due to the shorter exposure of the ground to the solar irradiation; this results in less buoyancy-generated TKE and thus lower ABL height values [blue symbols in Fig. 8(a)] with respect to the baseline distribution during daytime conditions. By the same principle, higher values of $\overline{w'w'}$ (associated with higher values of ABL height) are found during MAM and JJA daytime periods [Figs. 8b and 8(c)], whereas negligible difference is found during SON. By contrast, before sunrise (i.e., before 16:00 UTC) no qualitative difference is found in the daily averaged values of z_i within the seasons with respect to the baseline trend.

The impact of seasonal trends on the ABL height is further examined by calibrating the models of Eqs. (7) and (9) for stable conditions and the model of Eq. (10) for convective conditions over different
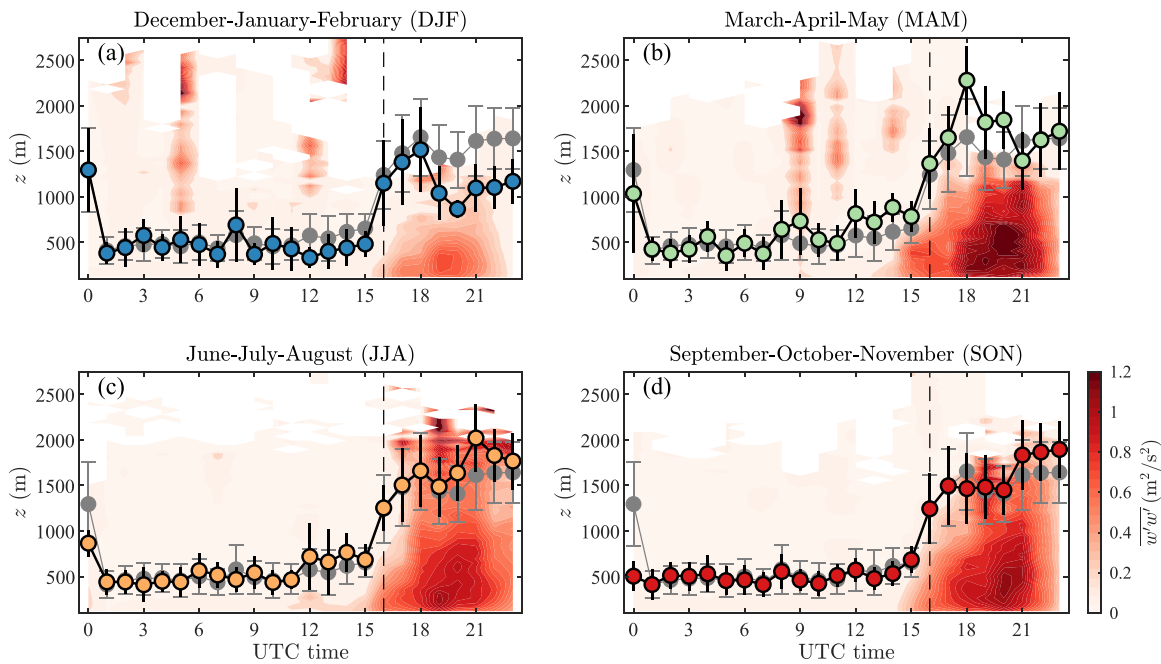

FIG. 7. Daily cycle of ABL height calculated during different seasons (colored symbols) overlapped to the baseline ABL daily cycle (gray symbols) and vertical velocity variance.
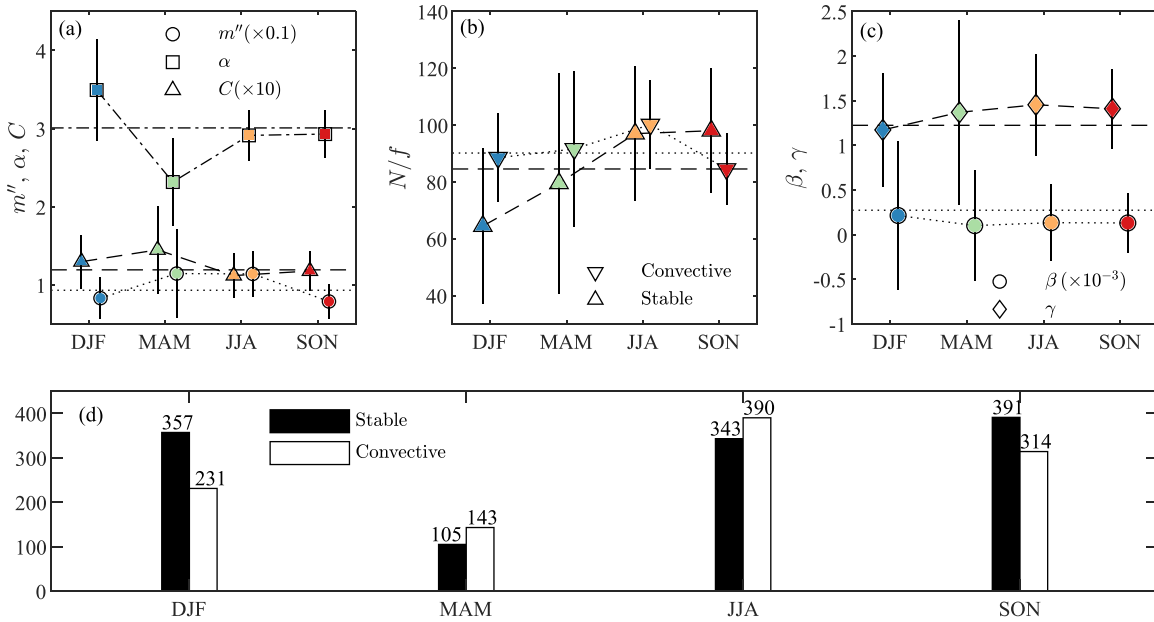
FIG. 8. Intra-annual variability of (a) models' multiplicative parameters (α, m'', C) (b) nondimensional Brunt–Väisälä frequency, and (c) β, γ. Panel (d) shows the available data points for each season bin for stable (black bars) and convective (white bars) conditions.

seasonal subsets. The fitted parameters are reported in Table II grouped by model and in Fig. 8 by physical effect. In particular, Fig. 8(a) depicts all the parameters directly impacted by any vertical displacement of the μ-z_i/L distribution (namely, m'', α, and C), which is deemed to be caused by the seasonal timescale. Figure 8(b) reports the averaged values of N/f across different seasons for both stable and convective conditions. Finally, Fig. 8(c) focuses on the parameters β, γ of Eq. (9).

Focusing on Fig. 8(a), the parameter α of Eq. (7) (reported with squared symbols) assumes higher value on DJF with respect to the reference (+16%, cf. with Table II), indicating a lower ABL height under stable conditions as compared to the averaged value across the year. By contrast, a sensibly lower α value (−23% from baseline) is found during MAM, followed by slightly lower values during JJA ((−3%) and SON ((−3%), which implies higher stable ABL height during these months. However, it should be noticed that the best fit for the MAM bin relies on fewer data points as compared to the other bins, as reported by Fig. 8(d). This implies larger fitting uncertainty and thus

less reliable values for the MAM period. These considerations are less evident when observing C, for which the uncertainty intervals associated with the fitting do not allow for firm conclusions of the seasonal trend [cf. with Fig. 8(a), triangular symbols]. Finally, the seasonal distribution of m'' (thus focused on convective conditions) confirms the previously mentioned qualitative result, i.e., lower convective ABL height during DJF with respect to the year average modeled by a lower value of m'' (−11%), and higher ABL heights (thus higher m'') during MAM (+23% increase in m'') and JJA (+13% increase) and, finally, lower ABL heights during SON (−15%). In conclusion, it is inferred that the effect of seasonal timescales on the ABL height is embedded into the model parameters α (for stable conditions) and m'' (for convective conditions), whereas the parameter C is less sensitive to the seasonal variability.

The seasonal trends of nondimensional Brunt–Väisälä frequency obtained by calibrating Eq. (7) in stable conditions and Eq. (10) in convective conditions exhibit overlapping intervals ($64 \leq N/f \leq 97$ in stable conditions and $85 \leq N/f \leq 100$ in convective conditions).

TABLE II. Calibration of different ABL height models across different seasons. The values in parenthesis quantify the percentage difference with respect to the baseline values (reported in Table I).

	Ref. 12 (Eq. 10)		Ref. 18 (Eq. 7)		Present model [Eq. (9)]		
	m''	$\dfrac{N}{f}$ ($L<0$)	α	$\dfrac{N}{f}$ ($L>0$)	C	β ($\times10^{-3}$)	γ
DJF	8.3 (−11%)	88 (−2%)	3.49 (+16%)	64 (−24%)	0.13 (+9%)	2.15 (−22%)	1.17 (−4%)
MAM	11.5 (+23%)	92 (+2%)	2.32 (−23%)	80 (−6%)	0.14 (+22%)	1.02 (−63%)	1.37 (+12%)
JJA	11.4 (+13%)	100 (+11%)	2.91 (−3%)	97 (+15%)	0.11 (−6%)	1.34 (−51%)	1.45 (+19%)
SON	7.9 (−15%)	85 (−6%)	2.93 (−3%)	98 (+16%)	0.12 (−1%)	1.31 (−52%)	1.41 (+15%)

However, while the Brunt–Väisälä frequency is nearly constant across different bins for convective conditions, the analogous frequency in stable conditions shows a peak during JJA and SON [as reported in Fig. 8(b)]. The uncertainty intervals obtained for the MAM data [green symbols in Fig. 8(b)] are sensibly larger than the other estimates, again due to the lower number of data points available.

Finally, the seasonal trend of γ [reported in Fig. 8(c) with diamond symbols] reveals a slight increase from DJF (–4% with respect to the baseline) to SON (+15%). However, the large uncertainty intervals do not allow for further considerations about the growth rate of z_i during stable conditions across different seasons. Similarly, the uncertainty intervals around β do not allow for definitive conclusions on the effect of seasonal scales.

V. CONCLUSION

In this work, the ABL height (z_i) is quantified during the year-long AWAKEN campaign. Based on time series of vertical velocity and range-corrected signal-to-noise ratio probed by a vertically pointing scanning pulsed Doppler LiDAR, the ABL height is systematically evaluated for over 2200 quality-controlled 10-min averaged measurements. Two different diagnostic models are used to quantify the ABL height under convective and stable conditions. One model performs best under daytime conditions (i.e., when a well-mixed layer is ingrained in the ABL), and the other model performs best during nighttime low-turbulent conditions. This approach provides the complete coverage of the ABL height evolution throughout the diurnal cycle. The average daily variation agrees well with previous literature results and with the daily cycle of vertical velocity variance.

The simultaneous availability of two co-located 3D sonic anemometers allows us to provide quantitative information on the shear- and buoyancy-generated turbulence near the ground, thereby relating the ABL height variability to the near-ground thermal stability and shear turbulence. Similarly, the free-atmosphere stability (expressed by the Brunt–Väisälä frequency, N) is quantified based on the radiosonde potential temperature profiles available from the neighboring ARM SGP C1 site. Five stability-dependent ABL height models are introduced to capture the ABL height variability over a wide range of stability classes, the latter ranging within three orders of magnitude both for stable and convective conditions. One model (first proposed by Kitaigorodskii and Joffre[12]) is used to assess the ABL height in convective conditions, while four models are introduced for stable conditions. Among the latter, three models are taken from the literature, namely, from the Zilitinkevich and Mironov,[16] Joffre et al.,[13] and Steeneveld et al.[18] studies, while the last model is introduced here to generalize the geostrophic drag law originally proposed by Rossby and Montgomery.[60] It is noteworthy that the Brunt–Väisälä frequency is fitted on the data as a free parameter for the models of Kitaigorodskii and Joffre[12] and Steeneveld et al.,[18] and it is subsequently validated against radiosonde measurements collected at the ARM SGP C1 site (located nearly 30 km north of the tested site). Good agreement is inferred for the Kitaigorodskii and Joffre,[12] Steeneveld et al.,[18] and proposed model with respect to the experimental ABL height estimates. By contrast, low agreement is obtained between the retrieved ABL heights against the Zilitinkevich and Mironov[16] and Joffre et al.[13] predictions. From a quantitative standpoint, the models' parameters match well with the analogous values found in the literature. Similarly, the fitted values of the Brunt–Väisälä frequency in convective ($N/f = 90$, where f is the Coriolis parameter) and stable ($N/f = 85$)

conditions agree well with the analogous intervals obtained from radiosonde measurements ($50 \leq N/f \leq 200$ and $100 \leq N/f \leq 350$ for convective and stable stratification, respectively).

Finally, the variability of each model's fitting parameters is physically linked to intra-annual timescales by fitting the models over non-overlapping seasonal subsets. In particular, the lower TKE buoyancy production (due to shorter periods of solar irradiance on the ground) during the winter season induces lower ABL height, as opposed to spring and summer seasons. This effect is carried on by each model's multiplicative constant, for which the intra-annual distributions are found to agree with the seasonal cycle of TKE buoyancy production.

AUTHOR DECLARATIONS
Conflict of Interest

The authors have no conflicts to disclose.

Author Contributions

M. Puccioni: Conceptualization (equal); Data curation (equal); Formal analysis (equal); Investigation (equal); Methodology (equal); Software (equal); Writing – original draft (equal); Writing – review & editing (equal). **C. F. Moss:** Investigation (equal); Methodology (equal). **M. S. Solari:** Investigation (equal); Methodology (equal). **S.**

Roy: Investigation (equal); Methodology (equal). **G. V. Iungo:** Funding acquisition (equal); Investigation (equal); Methodology (equal); Supervision (equal). **S. Wharton:** Funding acquisition (equal); Project administration (equal); Supervision (equal). **P. Moriarty:** Funding acquisition (equal); Project administration (equal); Supervision (equal).

DATA AVAILABILITY

The lidar data collected during the pre-campaign test are available at www.a2e.energy.gov.

APPENDIX A: THE WAVELET COVARIANCE TRANSFORM METHOD

The wavelet covariance transform (WCT) method, introduced by Davis et al.[29] and Brooks[30] and further elaborated by Baars et al.,[67] is an algorithm to detect sharp transitions in a chosen function, $f(z)$, based on the local functional values. In particular, the function is convoluted with the wavelet Haar function (h):

$$\text{WCT}(a, b) = \frac{1}{a} \int_{z_{\min}}^{z_{\max}} f(z) h\left(\frac{z - b}{a}\right) dz, \tag{A1}$$

where $z_{\min}, z_{\max}$ are the lowest and highest probed heights, respectively. In this work, we select $f(z) = z^2\text{SNR}$ (see Sec. III B for further details). The Haar function is piecewise defined based on the dilation (a) and translation (b) parameters as follows:

$$h\left(\frac{z - b}{a}\right) = \begin{cases} 1, & b - \frac{a}{2} \leq z < b \\ -1, & b \leq z < b + \frac{a}{2}, \\ 0 & \text{otherwise} \end{cases} \tag{A2}$$

and reported in Fig. 9(a) with a red line. It can be shown that, as b changes (and, thus, h is translated along z), the WCT attains a local maximum within a sharp interval, whereas it decreases outside of it. The ABL height is then found as

$$z_i(a) = \max_b[\text{WCT}(a, b)]. \tag{A3}$$

In this work, b is assumed equal to the LiDAR range gate values within $z_{\min} = 500$ and $z_{\max} = 3500$ m, thus with increase equal to the range gate (48 m).

As evidenced by Eq. (A3), the correct quantification of z_i relies on a correct choice of dilation parameter, a, which is physically associated with the depth of the entrainment zone. In particular, a relatively low value of a (≈ 100 m) is sensitive to the noise fluctuations of $z^2\text{SNR}$, whereas a large value of a ($\approx 10^3$ m) may exceed the entrainment zone depth, and thus, the local maximum of the WCT would be smoothed out by the convolution integral. In this work, the correct value of a is found by the iterative procedure introduced by Brooks.[30] A large dilation parameter ($a_0 = 2000$ m) is initially guessed to obtain a first estimate of the WCT (said WCT_0), the latter attaining a peak value ($\text{WCT}_{\max,0}$) for a certain translation parameter, b_0, and reducing to a fraction of the maximum value (here assumed $0.3\text{WCT}_{\max,0}$) within a certain interval Δb_0 centered around b_0 [cf. with Fig. 8(b)]. Since the WCT is nearly zero outside of the entrainment zone, Δb_0 is assumed as a proxy of the entrainment zone depth[30] and, thus, can be used as a better estimate of the dilation parameter for the next iteration ($a_1 = \Delta b_0$). The iterative procedure ends when the percentage difference between a_i and Δb_{i-1} (where i is the iteration number) is less than 10% or when the number of iterations reaches 100.

APPENDIX B: ASSESSMENT OF THE QUALITY CONTROL OF 3D SONIC DATA

The quality control process detailed in Sec. II B is designed to satisfy two contrasting requirements, i.e., having the largest number of quality-controlled 3D sonic statistics as possible and, on the other hand, minimizing the detrimental effect of large statistical
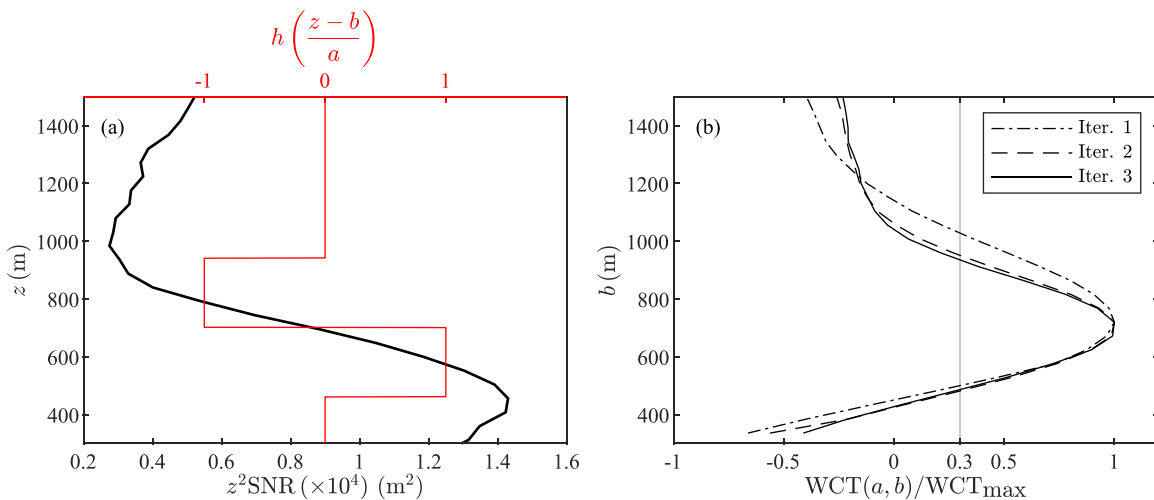

FIG. 9. Summary of wavelet covariance transform (WCT) method. (a) Haar function (red line) and range-corrected SNR (black line); (b) WCT(a, b) through different iterations with reduced dilation parameter relative to the maximum value; the vertical gray line indicates the threshold used to update the dilation parameter (0.3).
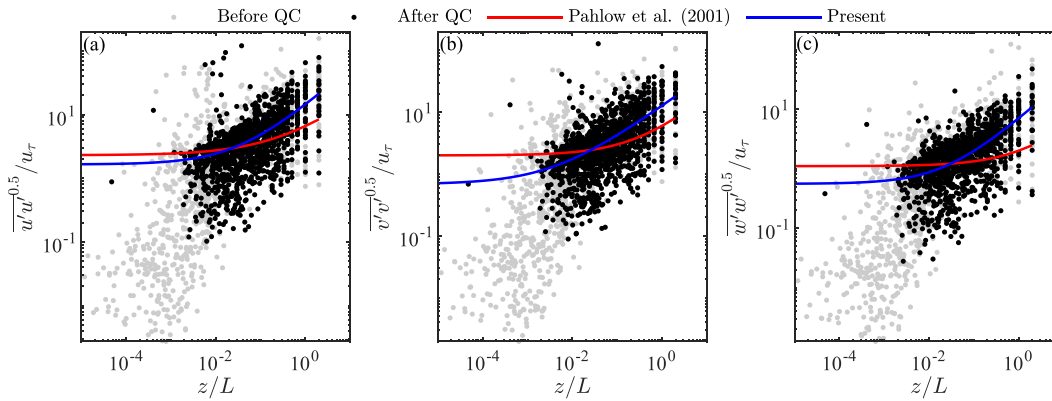
FIG. 10. Stability dependence of each velocity component's standard deviation retrieved from 3D sonic data before (gray symbols) and after (black symbols) the quality control detailed in Sec. II B. (a) Streamwise velocity component; (b) spanwise velocity component; (c) vertical velocity component. The red lines represent Eq. (B1) with the constants provided by Ref. 71, while the blue lines represent Eq. (B1) calibrated on the present data.

TABLE III. Comparison between the MOST similarity function parameters calibrated by Pahlow *et al.*[71] and the ones calibrated on the present data.

Equation (B1) parameters	a		B		c	
Velocity component	Ref. 71	Present	Ref. 71	Present	Ref. 71	Present
Streamwise (u)	2.3	2.1	4.3	14.4	0.5	0.6
Spanwise (v)	2.0	1.0	4.0	13.6	0.6	0.5
Vertical (w)	1.1	0.7	0.9	7.3	0.6	0.7

uncertainty in the data. In this scenario, the Monin–Obukhov similarity theory (MOST) has been leveraged to assess the effectiveness of the quality control process on the 3D sonic data. In particular, for stably stratified flows, the standard deviation of each velocity component can be modeled as a polynomial function of the stability parameter z/L as follows:[71–73]

$$\frac{\overline{u_i' u_i'}^{0.5}}{u_\tau} = a_i + b_i \left(\frac{z}{L}\right), \quad (B1)$$

where the subscript "i" refers to each velocity component ($i = 1, 2, 3$ corresponding to u, v, and w, respectively); for the present work, the sonic anemometer height is: $z = 2$ m. Thus, Eq. (B1) is utilized as a reference against which the quality-controlled sonic statistics are validated. The shear-corrected velocity standard deviations obtained from the 3D sonic anemometer data are plotted against the stability parameter z/L (see Fig. 10) before (gray symbols in Fig. 10) and after (black symbols in Fig. 10) the quality control procedure. Here, it is observed that the quality control algorithm is particularly effective in removing the data characterized by extremely low values of stability parameters ($z/L \leq 0.01$). These data are characterized by low values of sensible heat flux ($\overline{w'\theta'}$), which, in turn, reflects into high values of Obukhov length. In this situation, even a small statistical uncertainty on the sensible heat flux can cause a large uncertainty in the estimation of the Obukhov length; thus, the quality control procedure rejects these data. Indeed, we observe a strong disagreement comparing the rejected data with $z/L \leq 0.01$ against the MOST prediction (red lines in Fig. 10).

The best fit of Eq. (B1) (whose parameters are reported in Table III for each velocity component) on the present quality-controlled data captures the increase in shear-corrected standard deviation with the stability parameters, as well as the plateau as z/L goes to 0. Comparing the best-fitted quantities with the reference values, the largest source of discrepancy is found in the values of b (Table III). This could be explained considering the lack of data beyond $z/L = 2$, as opposed to the dataset shown by Pahlow *et al.* reaching $z/L = 10$; this leads to a less precise calibration of the second term on the right-hand side of Eq. (B1), which models the increase in shear-corrected standard deviation with the stability. However, the 3D sonic velocity statistics remaining from the quality control procedure agree with the MOST prediction, whereas the rejected portion of the data does not. Thus, it is concluded that the adopted quality control process leads to a reliable quantification of the turbulence state close to the ground.

REFERENCES

[1] R. B. Stull, *An Introduction to Boundary Layer Meteorology* (Springer Science & Business Media, 1988), Vol. 13.

[2] J. R. Garratt, *The Atmospheric Boundary Layer* (Elsevier, 1994), Vol. 37.

[3] J. Quan, Y. Dou, X. Zhao, Q. Liu, Z. Sun, Y. Pan, X. Jia, Z. Cheng, P. Ma, J. Su *et al.*, "Regional atmospheric pollutant transport mechanisms over the North China Plain driven by topography and planetary boundary layer processes," Atmos. Environ. **221**, 117098 (2020).

[4] A. R. Brown, R. J. Beare, J. M. Edwards, A. P. Lock, S. J. Keogh, S. F. Milton, and D. N. Walters, "Upgrades to the boundary-layer scheme in the met office numerical weather prediction model," Boundary-Layer Meteorol. **128**, 117–132 (2008).

[5]Z. Li, J. Guo, A. Ding, H. Liao, J. Liu, Y. Sun, T. Wang, H. Xue, H. Zhang, and B. Zhu, "Aerosol and boundary-layer interactions and impact on air quality," Natl. Sci. Rev. **4**, 810–833 (2017).

[6]R. J. A. M. Stevens and C. Meneveau, "Flow structure and turbulence in wind farms," Annu. Rev. Fluid Mech. **49**, 311–339 (2017).

[7]C. M. Jubayer and H. Hangan, "A numerical approach to the investigation of wind loading on an array of ground mounted solar photovoltaic (PV) panels," J. Wind Eng. Ind. Aerodyn. **153**, 60–70 (2016).

[8]J. C. Wyngaard, "Atmospheric turbulence," Annu. Rev. Fluid Mech. **24**, 205–234 (1992).

[9]J. C. Kaimal and J. J. Finnigan, *Atmospheric Boundary Layer Flows: Their Structure and Measurement* (Oxford University Press, 1994).

[10]A. Burgos-Cuevas, A. Magaldi, D. K. Adams, M. Grutter, J. L. García Franco, and A. Ruiz-Angulo, "Boundary layer height characteristics in Mexico City from two remote sensing techniques," Boundary-Layer Meteorol. **186**, 287–304 (2023).

[11]R. Krishnamurthy, R. K. Newsom, D. Chand, and W. J. Shaw, "Boundary layer climatology at ARM Southern Great Plains," Technical Report No. PNNL-30832 (PNNL, 2021).

[12]S. Kitaigorodskii and S. M. Joffre, "In search of a simple scaling for the height of the stratified atmospheric boundary layer," Tellus A **40A**, 419–433 (1988).

[13]S. M. Joffre, M. Kangas, M. Heikinheimo, and S. A. Kitaigorodskii, "Variability of the stable and unstable atmospheric boundary-layer height and its scales over a boreal forest," Boundary-Layer Meteorol. **99**, 429–450 (2001).

[14]S. A. Kitaigorodskii, "On the computation of the thickness of the wind-mixing layer in the ocean," Bull. Acad. Sci. USSR Geophys. Ser. **3**, 284–287 (1960).

[15]S. S. Zilitinkevich, "On the determination of the height of the Ekman boundary layer," Boundary-Layer Meteorol. **3**, 141–145 (1972).

[16]S. Zilitinkevich and D. V. Mironov, "A multi-limit formulation for the equilibrium depth of a stably stratified boundary layer," Boundary-Layer Meteorol. **81**, 325–351 (1996).

[17]F. T. M. Nieuwstadt, "The steady-state height and resistance laws of the nocturnal boundary layer: Theory compared with Cabauw observations," Boundary-Layer Meteorol. **20**, 3–17 (1981).

[18]G. J. Steeneveld, B. J. H. Van de Wiel, and A. A. M. Holtslag, "Diagnostic equations for the stable boundary layer height: Evaluation and dimensional analysis," J. Appl. Meteorol. Climatol. **46**, 212–225 (2007).

[19]R. T. Pollard, P. B. Rhines, and R. O. R. Y. Thompson, "The deepening of the wind-mixed layer," Geophys. Fluid Dyn. **4**, 381–404 (1973).

[20]S. Zilitinkevich and P. Calanca, "An extended similarity theory for the stably stratified atmospheric surface layer," Q. J. R. Meteorol. Soc. **126**, 1913–1923 (2000).

[21]D. Cheng-Ying, G. Zhi-Qiu, W. Qing, and C. Gang, "Analysis of atmospheric boundary layer height characteristics over the arctic ocean using the aircraft and GPS soundings," Atmos. Oceanic Sci. Lett. **4**, 124–130 (2011).

[22]D. Vickers and L. Mahrt, "Evaluating formulations of stable boundary layer height," J. Appl. Meteorol. Climatol. **43**, 1736–1749 (2004).

[23]G. S. Poulos, W. Blumen, D. C. Fritts, J. K. Lundquist, J. Sun, S. P. Burns, C. Nappo, R. Banta, R. Newsom, J. Cuxart *et al.*, "CASES-99: A comprehensive investigation of the stable nocturnal boundary layer," Bull. Am. Meteorol. Soc. **83**, 555–582 (2002).

[24]J. K. Lundquist, J. M. Wilczak, R. Ashton, L. Bianco, W. A. Brewer, A. Choukulkar, A. Clifton, M. Debnath, R. Delgado, K. Friedrich *et al.*, "Assessing state-of-the-art capabilities for probing the atmospheric boundary layer: The XPIA field campaign," Bull. Am. Meteorol. Soc. **98**, 289–314 (2017).

[25]P. Seibert, F. Beyrich, S. E. Gryning, S. M. Joffre, A. Rasmussen, and P. Tercier, "Review and intercomparison of operational methods for the determination of the mixing height," Atmos. Environ. **34**, 1001–1027 (2000).

[26]J. B. Duncan, Jr., L. Bianco, B. Adler, T. Bell, I. V. Djalalova, L. Riihimaki, J. Sedlar, E. N. Smith, D. D. Turner, T. J. Wagner *et al.*, "Evaluating convective planetary boundary layer height estimations resolved by both active and passive remote sensing instruments during the CHEESEHEAD19 field campaign," Atmos. Meas. Tech. **15**, 2479–2502 (2022).

[27]D. G. Steyn, M. Baldi, and R. M. Hoff, "The detection of mixed layer depth and entrainment zone thickness from lidar backscatter profiles," J. Atmos. Oceanic Technol. **16**, 953–959 (1999).

[28]S. A. Cohn and W. M. Angevine, "Boundary layer height and entrainment zone thickness measured by lidars and wind-profiling radars," J. Appl. Meteorol. Climatol. **39**, 1233–1247 (2000).

[29]K. J. Davis, N. Gamage, C. R. Hagelberg, C. Kiemle, D. H. Lenschow, and P. P. Sullivan, "An objective method for deriving atmospheric structure from airborne lidar observations," J. Atmos. Oceanic Technol. **17**, 1455–1468 (2000).

[30]I. M. Brooks, "Finding boundary layer top: Application of a wavelet covariance transform to lidar backscatter profiles," J. Atmos. Oceanic Technol. **20**, 1092–1105 (2003).

[31]S. Emeis, K. Schäfer, and C. Münkel, "Surface-based remote sensing of the mixing-layer height—A review," Meteorol. Z. **17**, 621 (2008).

[32]W. Kong and F. Yi, "Convective boundary layer evolution from lidar backscatter and its relationship with surface aerosol concentration at a location of a central China megacity," J. Geophys. Res. **120**, 7928–7940, https://doi.org/10.1002/2015JD023248 (2015).

[33]L. Menut, C. Flamant, J. Pelon, and P. H. Flamant, "Urban boundary-layer height determination from lidar measurements over the Paris area," Appl. Opt. **38**, 945–954 (1999).

[34]L. Kristensen, D. H. Lenschow, P. Kirkegaard, and M. Courtney, "The spectral velocity tensor for homogeneous boundary-layer turbulence," Boundary-Layer Meteorol. **47**, 149–193 (1989).

[35]H. A. Panofsky and J. A. Dutton, *Atmospheric Turbulence. Models and Methods for Engineering Applications* (Wiley, New York, 1984).

[36]J. W. Melgarejo and J. W. Deardorff, "Stability functions for the boundary-layer resistance laws based upon observed boundary-layer heights," J. Atmos. Sci. **31**, 1324–1333 (1974).

[37]Y. L. Pichugina and R. M. Banta, "Stable boundary layer depth from high-resolution measurements of the mean wind profile," J. Appl. Meteorol. Climatol. **49**, 20–35 (2010).

[38]Y. Zhang, Z. Gao, D. Li, Y. Li, N. Zhang, X. Zhao, and J. Chen, "On the computation of planetary boundary-layer height using the bulk Richardson number method," Geosci. Model Dev. **7**, 2599–2611 (2014).

[39]H. A. Cleugh and C. S. B. Grimmond, "Modelling regional scale surface energy exchanges and CBL growth in a heterogeneous, urban-rural landscape," Boundary-Layer Meteorol. **98**, 1–31 (2001).

[40]B. Hennemuth and A. Lammert, "Determination of the atmospheric boundary layer height from radiosonde and lidar backscatter," Boundary-Layer Meteorol. **120**, 181–200 (2006).

[41]T. Gal-Chen, M. Xu, and W. L. Eberhard, "Estimations of atmospheric boundary layer fluxes and other turbulence parameters from doppler lidar data," J. Geophys. Res. **97**, 18409–18423, https://doi.org/10.1029/91JD03174 (1992).

[42]R. Dang, Y. Yang, X.-M. Hu, Z. Wang, and S. Zhang, "A review of techniques for diagnosing the atmospheric boundary layer height (ABLH) using aerosol lidar data," Remote Sens. **11**, 1590 (2019).

[43]R. Frehlich, S. M. Hannon, and S. W. Henderson, "Coherent Doppler lidar measurements of wind field statistics," Boundary-Layer Meteorol. **86**, 233–256 (1998).

[44]S. Liu and X. Z. Liang, "Observed diurnal cycle climatology of planetary boundary layer height," J. Clim. **23**, 5790–5809 (2010).

[45]T. Luo, R. Yuan, and Z. Wang, "Lidar-based remote sensing of atmospheric boundary layer height over land and ocean," Atmos. Meas. Tech. **7**, 173–182 (2014).

[46]T. Su, Z. Li, and R. Kahn, "A new method to retrieve the diurnal variability of planetary boundary layer height from lidar under different thermodynamic stability conditions," Remote Sens. Environ. **237**, 111519 (2020).

[47]J. R. Lewis, E. J. Welton, A. M. Molod, and E. Joseph, "Improved boundary layer depth retrievals from MPLNET," J. Geophys. Res. **118**, 9870–9879, https://doi.org/10.1002/jgrd.50570 (2013).

[48]A. Peña, S. E. Gryning, and C. B. Hasager, "Comparing mixing-length models of the diabatic wind profile over homogeneous terrain," Theor. Appl. Climatol. **100**, 325–335 (2010).

[49]P. Moriarty, N. Bodini, P. Brugger, L. Goldberger, T. Herges, B. Hirth, G. V. Iungo, H. Ivanov, C. Kaul, P. Klein, R. Krishnamurthy, S. Letizia, K. Lundquist, V. R. Morris, R. Newsom, M. Pekour, A. Scholbrock, J. Schroeder, E. Simley, S. Wharton, and D. Zalkind, "Overview of Preparation for the American Wake Experiment (AWAKEN)," J. Renewable Sustainable Energy (in press) (2023).

[50]M. Debnath, P. Moriarty, R. Krishnamurthy, N. Bodini, R. Newsom, E. Quon, J. K. Lundquist, S. Letizia, G. V. Iungo, and P. Klein, "Characterization of wind speed and directional shear at the AWAKEN field campaign site," J. Renewable Sustainable Energy **15**, 033308 (2023).

28 October 2024 18:15:46

[51]M. Puccioni, G. V. Iungo, C. Moss, M. Shams Solari, S. Letizia, N. Bodini, and P. Moriarty, "LiDAR measurements to investigate farm-to-farm interactions at the AWAKEN experiment," J. Phys.: Conf. Ser. **2505**, 012045 (2023).

[52]C. Moss, R. Maulik, P. Moriarty, and G. V. Iungo, "Predicting wind farm operations with machine learning and the P2D-RANS model: A case study for an AWAKEN site," Wind Energy (published online) (2023).

[53]S. C. Tucker, C. J. Senff, A. M. Weickmann, W. A. Brewer, R. M. Banta, S. P. Sandberg, D. C. Law, and R. M. Hardesty, "Doppler lidar estimation of mixing height using turbulence, shear, and aerosol profiles," J. Atmos. Oceanic Technol. **26**, 673–688 (2009).

[54]S. Wu, B. Liu, J. Liu, X. Zhai, C. Feng, G. Wang, H. Zhang, J. Yin, X. Wang, R. Li *et al.*, "Wind turbine wake visualization and characteristics analysis by Doppler lidar," Opt. Express **24**, A762–A780 (2016).

[55]See https://adc.arm.gov/discovery/#/results/instrument_code::sondewnpn%2FdataLevel::b1 for E. Keeler, K. Burk, and J. Kyrouac, "Balloon-borne sounding system (sondewnpn)".

[56]J. M. Wilczak, S. P. Oncley, and S. A. Stage, "Sonic anemometer tilt correction algorithms," Boundary-Layer Meteorol. **99**, 127–150 (2001).

[57]L. H. Benedict and R. D. Gould, "Towards better uncertainty estimates for turbulence statistics," Exp. Fluids **22**, 129–136 (1996).

[58]R. K. Newsom and R. Krishnamurthy, "Doppler Lidar (DL) instrument handbook," Technical Report No. DOE/SC-ARM/TR-101 [DOE Office of Science Atmospheric Radiation Measurement (ARM) User Facility, 2022].

[59]H. Beck and M. Kühn, "Dynamic data filtering of long-range Doppler LiDAR wind speed measurements," Remote Sens. **9**, 561 (2017).

[60]C.-G. Rossby and R. B. Montgomery, "The layer of frictional influence in wind and ocean currents," Pap. Phys. Oceanogr. **3**, 1–101 (1935).

[61]S. P. S. Arya, "Geostrophic drag and heat transfer relations for the atmospheric boundary layer," Q. J. R. Meteorol. Soc. **101**, 147–161 (1975).

[62]N. P. Lareau, Y. Zhang, and S. A. Klein, "Observed boundary layer controls on shallow cumulus at the arm southern great plains site," J. Atmos. Sci. **75**, 2235–2255 (2018).

[63]J. G. Gebauer, E. Fedorovich, and A. Shapiro, "A 1D theoretical analysis of northerly low-level jets over the Great Plains," J. Atmos. Sci. **74**, 3419–3431 (2017).

[64]Y.-X. Yuan, *Trust Region Algorithms for Nonlinear Equations* (CiteSeer, 1994).

[65]A. G. M. Driedonks, "Models and observations of the growth of the atmospheric boundary layer," Boundary-Layer Meteorol. **23**, 283–306 (1982).

[66]C. Münkel, N. Eresmaa, J. Räsänen, and A. Karppinen, "Retrieval of mixing height and dust concentration with lidar ceilometer," Boundary-Layer Meteorol. **124**, 117–128 (2007).

[67]H. Baars, A. Ansmann, R. Engelmann, and D. Althausen, "Continuous monitoring of the boundary-layer top with lidar," Atmos. Chem. Phys. **8**, 7281–7296 (2008).

[68]D. Toledo, C. Córdoba-Jabonero, J. A. Adame, B. De La Morena, and M. Gil-Ojeda, "Estimation of the atmospheric boundary layer height during different atmospheric conditions: A comparison on reliability of several methods applied to lidar measurements," Int. J. Remote Sens. **38**, 3203–3218 (2017).

[69]G. de Arruda Moreira, F. J. da Silva Lopes, J. L. Guerrero-Rascado, M. J. Granados-Muñoz, R. Bourayou, and E. Landulfo, "Comparison between two algorithms based on different wavelets to obtain the planetary boundary layer height," Proc. SPIE. **9246**, 92460D (2014).

[70]A. Peña, S. E. Gryning, and C. B. Hasager, "Measurements and modelling of the wind speed profile in the marine atmospheric boundary layer," Boundary-Layer Meteorol. **129**, 479–495 (2008).

[71]M. Pahlow, M. B. Parlange, and F. Porté-Agel, "On Monin–Obukhov similarity in the stable atmospheric boundary layer," Boundary-Layer Meteorol. **99**, 225–248 (2001).

[72]A. A. Grachev, C. W. Fairall, P. O. G. Persson, E. L. Andreas, and P. S. Guest, "Stable boundary-layer scaling regimes: The SHEBA data," Boundary-Layer Meteorol. **116**, 201–235 (2005).

[73]I. Stiperski and M. Calaf, "Generalizing Monin-Obukhov similarity theory (1954) for complex atmospheric turbulence," Phys. Rev. Lett. **130**, 124001 (2023).

28 October 2024 18:15:46